**Cite this article**
Tarique O and Kovtun M (2022)
Novel one-part fly ash alkali-activated cements for ambient applications.
*Advances in Cement Research* **34(10)**: 458–471,
https://doi.org/10.1680/jadcr.21.00144

**Research Article**
**Paper 2100144**
Received 11/08/2021;
Accepted 11/04/2022;
Published online 10/06/2022



**Advances in Cement Research**

ice Publishing

# Novel one-part fly ash alkali-activated cements for ambient applications

**Oscar Tarique**
Postgraduate student, Department of Civil Engineering, University of Pretoria, Pretoria, Gauteng, South Africa

**Maxim Kovtun**
Senior Lecturer, Department of Civil Engineering, University of Pretoria, Pretoria, Gauteng, South Africa; Senior Materials Engineer, Sydney Water Corporation, Parramatta, New South Wales, Australia (Orcid:0000-0002-9594-3348) (corresponding author: maxim.kovtun@sydneywater.com.au)

**Alkali-activated cements utilising fly ash can be a low-carbon alternative to Portland cement. However, fly ash alkali-activated cements require curing at elevated temperature and have cost plus environmental implications owing to the use of strong alkali solutions. Unclassified fly ash, silica fume, calcium hydroxide and sodium carbonate were used to develop novel one-part fly ash alkali-activated cements. When cured at ambient conditions, the cements gained compressive strength up to 11.0 and 44.2 MPa at 3 and 28 days, respectively. Microstructural investigations revealed that cation exchange reaction between the activators was the key element in the development of the microstructure and strength of the cements. The novel fly ash alkali-activated cements have at least 50% lower impact on global warming than highly blended Portland cements.**

**Keywords:** alkali-activated cements/curing/fly ash (PFA)

## Notation

| | |
|---|---|
| $A$ | sodium carbonate ($Na_2CO_3$) (wt%) |
| $B$ | calcium hydroxide ($Ca(OH)_2$) (wt%) |
| $C$ | silica fume (wt%) |
| $Y$ | compressive strength (MPa) |

## Introduction

Coal-fired power plants form an integral part of energy sources for various countries, especially in South Africa. Eskom, one of the largest coal consumers in South Africa, uses approximately 109 million tonnes of coal per annum to generate electric energy. The company produces approximately 25 million tonnes of fly ash, a waste material, of which only 7% is then recycled (Eskom, 2021). The remainder is dumped in massive landfills. This has become a great concern because of numerous hazardous health and environmental impacts due to leaching of the ash's toxic heavy metals and trace elements (Jambhulkar *et al.*, 2018). It also contributes to the loss of useable land. The National Development Plan 2030 of South Africa, one of the country's most strategic initiatives, has placed specific attention on reducing the waste-to-landfill problem (National Planning Commission, 2017). To reduce the fly ash landfill issue, a nationwide need for its consumption and use must exist.

At the same time, significant emphasis is put on sustainable development through the use of materials with low environmental impact in the construction industry. This is primarily due to the continually increasing demand for the most resource and energy intensive products in the industry – Portland cement and concrete. Owing to their ecological aspects, there is a high demand for low-carbon cements. An attractive proposition is alkali-activated cements, which involve a chemical reaction between an aluminosilicate precursor and a strong alkali solution (Duxson *et al.*, 2007; Khale and Chaudhary, 2007).

Most of the fly ash utilised is sold to the cement industry because of its inherent cementitious properties. However, fly ash can also be used as a primary precursor for the production of alkali-activated materials (Khale and Chaudhary, 2007; Li *et al.*, 2010; Rashad, 2013). Fly ash alkali-activated materials are considered to be a low-carbon alternative for ordinary Portland cement (OPC) concretes. This drives the use of fly ash as a construction material because it will not only provide a greener alternative binder but will also assist in attaining the objective set out by the National Development Plan 2030.

Alkali-activated fly ash cements can gain high compressive strength and mechanical properties that are comparable to OPC (Olivia and Nikraz, 2012; Rangan, 2010; Ryu *et al.*, 2013). However, curing at elevated temperature is essential to reach the optimal mechanical characteristics for alkali-activated fly ash, because under ambient curing conditions it has a slow rate of dissolution and cannot attain satisfactory strength. Shekhovtsova *et al.* (2014) investigated the effects of sodium oxide concentration, the water-to-binder-solids ratio, temperature and duration of curing at elevated temperature on the compressive strength of alkali-activated cement pastes utilising Class F fly ash. The results of the investigation showed that curing at 25°C was a possibility, but not practical due to delayed setting, intensive efflorescence formation, very slow strength development (1.1 MPa at 7 days), relatively low strength (10 MPa) at 28 days and large strength deviation. Shekhovtsova *et al.* (2014) concluded that the optimal temperature was 60°C, because at 80°C excessive moisture loss caused a decrease in compressive strength at 91 days. The necessity of curing at elevated temperature limits

the use of alkali-activated fly ash cements to the precast industry and impedes their range of application. Unlike OPC concrete, which has freedom in curing conditions and can be cast on site, alkali-activated fly ash concrete requires controlled environments to be a useful alternative (Mustafa Al Bakria *et al.*, 2011; Rangan, 2010; Silva *et al.*, 2013).

The most commonly used alkali activators are sodium hydroxide and sodium silicates. These activators are expensive and cause safety issues pertaining to handling and storage due to their high pH. There are also concerns about environmental impacts from their manufacture (Habert *et al.*, 2011; McLellan *et al.*, 2011; Turner and Collins, 2013).

Thus, for fly ash alkali-activated cements to be able to convert a harmful waste material into a cost-effective and environmentally friendly building material, they need to be cured under ambient conditions, utilise activators with low environmental impact and the process to use the resulting material in the production of concrete should not deviate from current practices with OPC. In the present study, novel one-part fly ash alkali-activated cements comprising silica fume, calcium hydroxide and sodium carbonate are proposed.

To attain efficient synthesis of alkali-activated materials, source materials need to be combined in an effective manner (Part *et al.*, 2015). Pozzolanic materials require a source of lime to attain their cementitious properties, which can be provided by calcium hydroxide. However, for alkali-activated materials, a strong alkali medium is necessary for efficient dissolution of its aluminosilicate precursor for strength gain (Fraay *et al.*, 1989). Owing to the relatively low pH of calcium hydroxide, the activation of fly ash with calcium hydroxide has slow strength development. Fraay *et al.* (1989) demonstrated that a pH value of 13.3 was required for appropriate dissolution of alumina and silica species from fly ash particles. Therefore, an additive activator needs to be introduced to raise the pH of the system and promote early activation (Huang and Cheng, 1986; Li *et al.*, 2000).

To increase the pH, the addition of sodium carbonate, which has been used in the alkali activation of fly ashes (Abdalqader *et al.*, 2016; Jeon *et al.*, 2015), was considered. Sodium carbonate is a naturally occurring mineral and can be obtained from trona and sodium carbonate-rich brines or chemical processes such as the Solvay process. The worldwide total of naturally occurring sodium carbonate amounts to 24 billion tonnes (U. S. Geological Survey, 2017). Moreover, sodium carbonate is reported to be 2–3 times cheaper than sodium hydroxide or sodium silicates. In addition, to the low cost of this activator compared to the conventional ones, it is safer to handle and can yield lower drying shrinkage (Jin and Al-Tabbaa, 2015). Thus, the use of sodium carbonate as an activator can contribute to the development of more sustainable alkali-activated fly ash cements (Abdalqader *et al.*, 2016).

Silica fume is a highly reactive pozzolanic material because of its higher amorphous silicon dioxide content, as well as its very small particle size. Besides its high reactivity, silica fume can act as a filler material, which can fill in the voids of pores and aid in increasing mechanical strength by densification of the structure (Assi *et al.*, 2016; Dutta *et al.*, 2010; Songpiriyakij *et al.*, 2011). Owing to this nature, silica fume is highly reactive to calcium hydroxide, which can act to provide extra nucleation sites and aid in increasing mechanical strength, especially at early age, or can perform as a microfiller.

In most cases with alkali-activated materials, alkali solutions must be prepared in a controlled environment. On a construction site, the solutions can pose several health and safety concerns. However, in the proposed one-part fly ash alkali-activated cements, all the materials, including the activators, are dry and safer to handle. The novel cements can be stored in bags or silos, as would be in case with OPC, where the only component required to activate it is water.

The aim of the present study was to evaluate and report on the aptitude of the novel one-part fly ash alkali-activated cements cured under ambient conditions. To investigate and report the influence of each cement component on compressive strength development, a central composite design (CCD) was chosen to perform the statistical analysis. This was followed by studying the mineralogical and microstructural properties of selected cement pastes by conducting X-ray diffraction (XRD), Fourier transform infrared spectroscopy (FTIR) and scanning electron microscopy (SEM) analyses.

## Materials and experimental set-up

### Materials

Sodium carbonate (purity 99.0%), hydrated lime (purity 97.0%) and silica fume were procured from local distributors in South Africa. Unclassified low-calcium fly ash (class F) with the median particle size of 102.5 μm (Shekhovtsova, 2015) from Lethabo power station was used in the study. Sodium carbonate and hydrated lime were the activators, while silica fume and fly ash were the aluminosilicate precursors. Table 1 represents the chemical composition of the fly ash and silica fume which was determined by X-ray fluorescence (XRF) analysis.

Relative densities and greenhouse gas emissions measured in carbon dioxide equivalent ($CO_2$-e), of the materials are shown in Table 2. The greenhouse gas emission values were adopted from the Department of Industry, Science, Energy and Resources (2021) and the Infrastructure Sustainability Council of Australia (2021).

### Mathematical design of experiment

The procedure outlined by Montgomery and Runger (2011) was used to perform the statistical analysis. This included

**Table 1.** Chemical composition of materials (wt%)

| | $SiO_2$ | $TiO_2$ | $Al_2O_3$ | $Fe_2O_3$ | MgO | CaO | $Na_2O$ | $K_2O$ | $SO_3$ | Other | LOI |
|---|---|---|---|---|---|---|---|---|---|---|---|
| Fly ash | 56.23 | 1.57 | 30.67 | 4.45 | 0.49 | 4.54 | 0.27 | 0.81 | 0.37 | 0.31 | 0.28 |
| Silica fume | 88.86 | 0.01 | 0.60 | 4.63 | 1.03 | 1.86 | 0.28 | 2.03 | — | 0.22 | 4.58 |

Note: $SiO_2$, silicon dioxide; $TiO_2$, titanium dioxide; $Al_2O_3$, aluminium oxide; $Fe_2O_3$, iron (III) oxide; MgO, magnesium oxide; CaO, calcium oxide; $Na_2O$, sodium oxide; $K_2O$, potassium oxide; $SO_3$, sulfur trioxide

**Table 2.** Relative densities and greenhouse gas emissions

| | Sodium carbonate | Hydrated lime | Silica fume | Fly ash |
|---|---|---|---|---|
| Relative density | 2.54 | 2.32 | 2.30 | 2.23 |
| Emissions: kg $CO_2$-e/kg | 0.415 | 0.675 | 0.014 | 0.012 |

forming an initial model; conducting analysis of variance (ANOVA) tests; refining the model; analysing residuals; and interpreting results. The computer software Minitab 17.1.0 was used to assist in the design, analysis and interpretation of the $3^k$ face-centred CCD. CCDs allow for modelling and analysis of the response of interest as well as providing satisfactory information on the experimental variables and their effects plus error with a minimal number of runs.

A $3^k$ level face-centred CCD, with three centre point runs, was chosen with $\alpha = \pm 1$ as the region of interest encompassing the extremities. Coded/uncoded control variables and constant parameters are presented in Tables 3 and 4, respectively.

Coded cement designs are given in Table 5. The replication of the centre point runs provides an estimate of the experimental error (SC9|CH15|SF10, Table 5). The face-centred CCD was performed in random order to eliminate the possibility that one run depends on the conditions of the previous run or would have an influence on subsequent runs.

### Sample preparation and testing procedure

Fly ash, silica fume, calcium hydroxide and sodium carbonate were thoroughly mixed in the proportions indicated in Table 5. After mixing, the dry cements were stored in plastic bags until the date of casting.

Cement pastes were mixed in a Hobart mixer. Dry cement was added to a damp bowl and then water was added with the mixer running. Mixing was carried out for 5 min and then the mixer was stopped, and all leftover dry material was scraped off the bowl surface within 30 s. The mixer was run again for another 5 min until the cement paste was completely mixed.

Prismatic moulds were used to cast $40 \times 40 \times 160$ mm samples. The prepared cement pastes were placed in the moulds, compacted on a vibrating table, covered in a plastic film and left to set at $25 \pm 1$°C overnight. The samples were demoulded the following day and cured in a room with an ambient temperature of $25 \pm 1$°C and relative humidity of $85 \pm 5$%.

Compressive strength testing was carried out at 3, 7 and 28 days. Three half-prism samples were tested at each age. The

**Table 3.** Coded and uncoded values for control variables

| Control variables[a] | −1 | 0 | +1 |
|---|---|---|---|
| Calcium hydroxide: wt% | 10 | 15 | 20 |
| Sodium carbonate[b]: wt% | 6 | 9 | 12 |
| Silica fume: wt% | 5 | 10 | 15 |

[a]wt% = percentage of fly ash mass
[b]Calculated as a $Na_2O_{eq}$

**Table 4.** Constant parameters

| Parameter | Value |
|---|---|
| Curing conditions | $25 \pm 1$°C and relative humidity of $85 \pm 5$%. |
| Water-to-cement (*w*/*c*) ratio[a] | 0.27 |
| Cement paste mixing time | 10 min |

[a]Cement = fly ash + silica fume + calcium hydroxide + sodium carbonate

**Table 5.** Coded cement designs

| Cement ID[a] | SC | CH | SF |
|---|---|---|---|
| SC12\|CH20\|SF15 | +1 | +1 | +1 |
| SC12\|CH20\|SF5 | +1 | +1 | −1 |
| SC12\|CH10\|SF15 | +1 | −1 | +1 |
| SC12\|CH10\|SF5 | +1 | −1 | −1 |
| SC6\|CH20\|SF15 | −1 | +1 | +1 |
| SC6\|CH20\|SF5 | −1 | +1 | −1 |
| SC6\|CH10\|SF15 | −1 | −1 | +1 |
| SC6\|CH10\|SF5 | −1 | −1 | −1 |
| SC12\|CH15\|SF10 | +1 | 0 | 0 |
| SC6\|CH15\|SF10 | −1 | 0 | 0 |
| SC9\|CH20\|SF10 | 0 | +1 | 0 |
| SC9\|CH10\|SF10 | 0 | −1 | 0 |
| SC9\|CH15\|SF15 | 0 | 0 | +1 |
| SC9\|CH15\|SF5 | 0 | 0 | −1 |
| SC9\|CH15\|SF10 | 0 | 0 | 0 |
| SC9\|CH15\|SF10 | 0 | 0 | 0 |
| SC9\|CH15\|SF10 | 0 | 0 | 0 |

[a]SC – sodium carbonate; CH – calcium hydroxide; SF – silica fume; number represents weight percentage of fly ash mass

test procedure was conducted in accordance with SANS 50196-1 (SABS, 2006).

After being tested for compressive strength at 3 and 28 days, representative samples for selected cement pastes were collected and were dehydrated to prevent further material evolution. This was achieved by placing the samples in acetone to stop the reaction and then the samples were transferred to a vacuum chamber to filter out the acetone. Subsequently, the samples were placed in a desiccator at $25 \pm 1$°C to completely dry the sample until the testing date (Ismail *et al.*, 2013a, 2013b). To avoid overheating, samples for XRD and FTIR analyses were hand milled using a pestle and mortar.

The XRD samples were prepared according to the standardised PANalytical back-loading system, which provides nearly random distribution of the particles. The samples were analysed using a PANalytical X'Pert Pro powder diffractometer in $\theta$–$\theta$ configuration with an X'Celerator detector and variable divergence and fixed receiving slits with Fe filtered Co-K$\alpha$ radiation ($\lambda = 0.1789$ nm). The data were recorded in the angular range $5° < 2\theta < 90°$. Crystalline phases were identified using X'Pert Highscore Plus software.

The FTIR spectra of the selected samples were recorded on a solid state by a Vertex 70v spectrometer equipped with the Golden Gate diamond attenuated total reflectance cell (Bruker). The FTIR was recorded on the 4000–500 $cm^{-1}$ spectral region, with 32 acquisitions at a 4 $cm^{-1}$ resolution.

Samples for SEM analysis were fractured and coated with carbon. The SEM investigations were conducted on a Zeiss Ultra Plus FEM at an accelerating voltage of 1 kV.

## Results and discussion

### Statistical model and analysis

The strength development of the cement paste samples is shown in Figure 1.

The ANOVA was computed first to test the adequacy of the model. The *F*-value of the initial model was 52.41, implying that the model is significant, and the probability that this value was due to noise is less than 0.01%. Furthermore, the lack-of-fit *p*-value was 0.286, which indicates that it was insignificant as $p > 0.05$. The insignificance of the lack of fit implied that the model fitted the experimental data and the factors under consideration had a considerable impact on the response. However, there was an insignificant term in the model ($Na_2CO_3$*$Na_2CO_3$) which had a *p*-value of more than 0.05. The term was removed, and the reduced model ANOVA results are shown in Table 6.

The reduced model has an *F*-value of 65.34, which is greater than the initial model and still implies that the model is significant. Moreover, the lack of fit is still insignificant (*p*-value = $0.324 > 0.05$), which again shows the adequacy of the model.

Table 7 gives a comparison of the summary statistics for ANOVA of the initial model against the reduced model. The

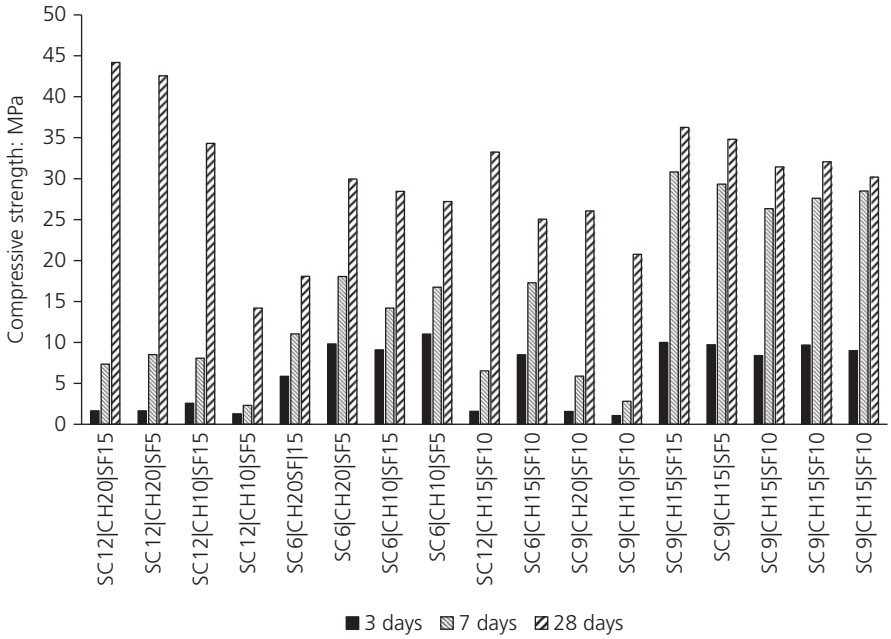


**Figure 1.** Strength development of proposed one-part fly ash alkali-activated cements

Table 6. Reduced ANOVA results

| Source | DF | Adj SS | Adj MS | *F*-value | *p*-value |
|---|---|---|---|---|---|
| Model | 8 | 970.2 | 121.3 | 65.34 | <0.0001 |
| Linear | 3 | 303.4 | 101.1 | 54.48 | <0.0001 |
| Sodium carbonate ($Na_2CO_3$) | 1 | 158.5 | 158.5 | 85.39 | <0.0001 |
| Calcium hydroxide ($Ca(OH)_2$) | 1 | 129.1 | 129.1 | 69.56 | <0.0001 |
| Silica fume | 1 | 15.78 | 15.78 | 8.50 | 0.019 |
| Square | 2 | 147.7 | 73.85 | 39.79 | <0.0001 |
| $Ca(OH)_2$*$Ca(OH)_2$ | 1 | 120.0 | 120.0 | 64.66 | <0.0001 |
| Silica fume*Silica fume | 1 | 102.9 | 102.9 | 55.46 | <0.0001 |
| Two-way interaction | 3 | 519.2 | 173.1 | 93.24 | <0.0001 |
| $Na_2CO_3$*$Ca(OH)_2$ | 1 | 263.1 | 263.1 | 141.8 | <0.0001 |
| $Na_2CO_3$*Silica fume | 1 | 131.1 | 131.1 | 70.61 | <0.0001 |
| $Ca(OH)_2$*Silica fume | 1 | 125.0 | 125.0 | 67.34 | <0.0001 |
| Error | 8 | 14.85 | 1.856 | | |
| Lack-of-fit | 6 | 13.03 | 2.172 | 2.39 | 0.324 |
| Pure error | 2 | 1.815 | 0.907 | | |
| Total | 16 | 985.1 | | | |

Table 7. Comparison between initial and reduced model

| Standard error | $R^2$ | $R^2$(adj) | $R^2$(pred) |
|---|---|---|---|
| Initial model | | | |
| 1.43450 | 0.9854 | 0.9666 | 0.8627 |
| Reduced model | | | |
| 1.36235 | 0.9849 | 0.9699 | 0.8812 |

$R^2$ of the reduced model indicates it can explain 0.9849 of the model's variability. The adjusted $R^2$ is 0.9699, which is relatively high and further emphasises the model's adequacy and that non-significant terms have not been included. The predicted $R^2$ is 0.8812, which shows the model's high predictive capability and confirms that the model has not been over-fit. It is also within the acceptable margin of 0.2 from the adjusted $R^2$ (StatEase Inc., 2021).

Analysis of residuals suggests there was no violation of the least-squares regression assumptions, which are normality, constant variance and independence. Residuals followed a straight line in the normal probability plot, which verified the assumption that the residuals were normally distributed. There were no visible trends in the residuals against fits graph. The vertical width of the scatter did not change significantly when moving along the fitted values, which shows that the assumption of residuals having a constant variance is reasonable. A plot of residuals against order fluctuated randomly across the centreline of the graph, showing the residuals were uncorrelated and the model was adequate.

With the model statistics and assumptions satisfied after analysis of the residuals, the final model can be used to navigate the design space. The final empirical model equation is given in Equations 1 and 2 as coded and actual units, respectively. Coded variables help with interpretation of the model and variable effects as the magnitude of the coefficients are given on a common scale.

$$Y = 30.200 + 3.981A + 3.593B + 1.256C - 6.259B^2 + 5.830C^2 + 5.735AB + 4.047AC - 3.952BC \quad (1)$$

where $Y$ is compressive strength (MPa); $A$ is sodium carbonate ($Na_2CO_3$) (wt%), $-1 \le A \le 1$; $B$ is calcium hydroxide ($Ca(OH)_2$) (wt%), $-1 \le B \le 1$; and $C$ is silica fume (wt%), $-1 \le C \le 1$.

$$Y = 23.82 - 7.106A + 6.410B - 4.471C - 0.2518B^2 + 0.2332C^2 + 0.3829AB + 0.2698AC - 0.1581BC \quad (2)$$

where, $Y$ is compressive strength (MPa); $A$ is sodium carbonate ($Na_2CO_3$) (wt%), $6 \le A \le 12$; $B$ is calcium hydroxide ($Ca(OH)_2$) (wt%), $10 \le B \le 20$; and $C$ is silica fume (wt%), $5 \le C \le 15$.

## Influence of cement components on compressive strength

The response surface plots are shown in Figure 2 at different levels of silica fume content.

All three independent variables positively contribute to compressive strength development (Equation 1 and Figure 2). Both calcium hydroxide and sodium carbonate contribute a significant portion, with sodium carbonate being the most dominant. It is also worth noting that the interaction of calcium hydroxide and sodium carbonate is a major contributor to the gain in compressive strength. Fraay *et al.* (1989) showed that highly alkaline solutions with pH over 13.3 were required for rapid dissolution of the amorphous phase of class F fly ash to leach alumina and silica species. Both calcium hydroxide and sodium carbonate provide lower pH values (Fernández-Jiménez and Puertas, 2003; Huang and Cheng, 1986).

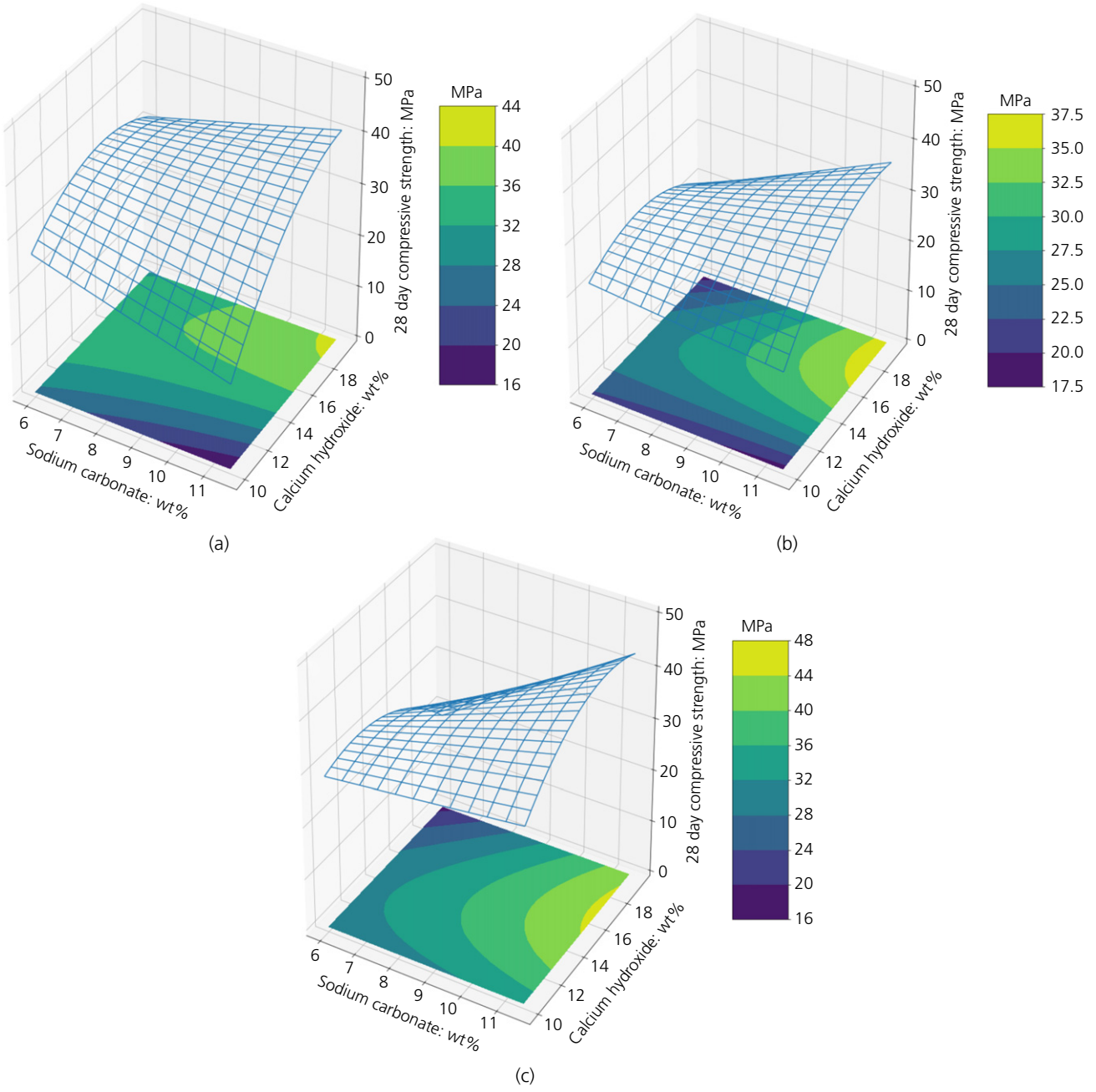


**Figure 2.** Response surface plots at constant silica fume: (a) 5 wt%; (b) 10 wt%; (c) 15 wt%

However, the cation reaction between calcium hydroxide and sodium carbonate significantly increases the pH of the system through the formation of gaylussite and subsequently calcium carbonate (see next section 'XRD analysis'). The increased alkalinity promotes the dissolution of fly ash particles, releasing alumina and silica species which participate in the formation of calcium silicate hydrates (C–S–H) (Shi and Day, 2000). Calcium carbonate, which is one of the final products of the cation exchange reaction, has a pore-refining effect that can reduce the porosity and promote better mechanical strength. Fine calcium carbonate also has a seeding effect that could promote early C–S–H gel formation to improve strength (Rashad and Khalil, 2013; Sato and Beaudoin, 2011). Therefore, samples that contained the highest content of sodium carbonate and calcium hydroxide generally obtained higher compressive strength at 28 days.

It was found that silica fume provides a beneficial effect on the compressive strength by creating a more compact microstructure and greater formation of reaction products during alkali

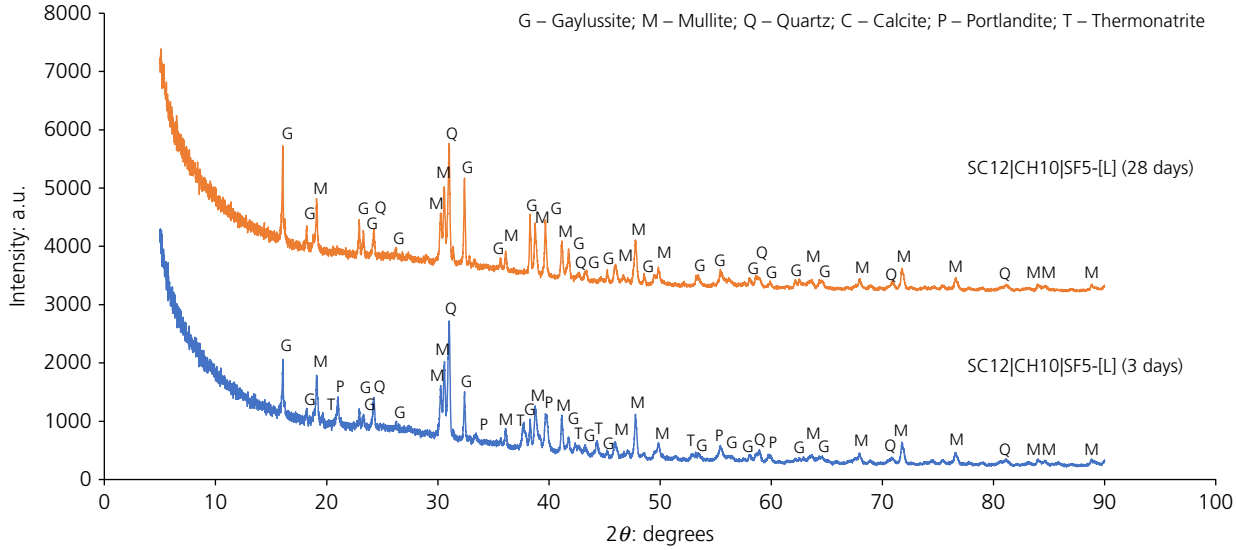


**Figure 3.** XRD patterns of SC12|CH10|SF5-[L] cement paste

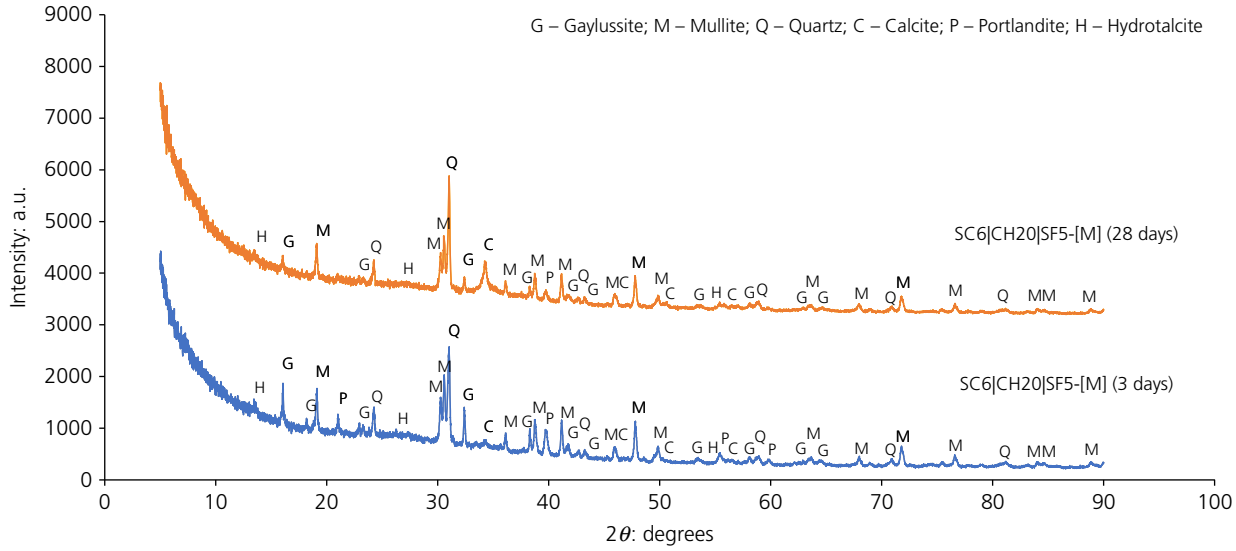


**Figure 4.** XRD patterns of SC6|CH20|SF5-[M] cement paste

activation (Assi *et al.*, 2016; Rashad and Khalil, 2013; Sayed and Zeedan, 2012; Songpiriyakij *et al.*, 2011). However, it can be observed that its effect is noticeably smaller when compared to sodium carbonate and calcium hydroxide, albeit still positive (Equation 1). It might be argued that the highly reactive nature of silica fume could have played a role in promoting activation under ambient conditions. Jeon *et al.* (2015) studied a blend of fly ash, calcium hydroxide and sodium carbonate that was cured at 60°C, which attained a compressive strength of 36 MPa at 28 days. In comparison, the highest compressive strength achieved by the one-part fly ash alkali-activated cements under ambient conditions was 44.2 MPa at 28 days.

To evaluate the microstructural and mineralogical changes that occurred in the developed one-part fly ash alkali-activated cements over time, three cement paste samples were selected. The selected samples were SC12|CH10|SF5-[L], SC6|CH20|SF5-[M] and SC12|CH20|SF5-[H], which gained low [L], moderate [M] and high [H] strength at 28 days, respectively.

## XRD analysis

The XRD patterns for the SC12|CH10|SF5-[L], SC6|CH20|SF5-[M] and SC12|CH20|SF5-[H] samples are shown in Figures 3–5. The XRD pattern of the fly ash can be found in figure 3.4 (Lethabo I) of Shekhovtsova (2015).

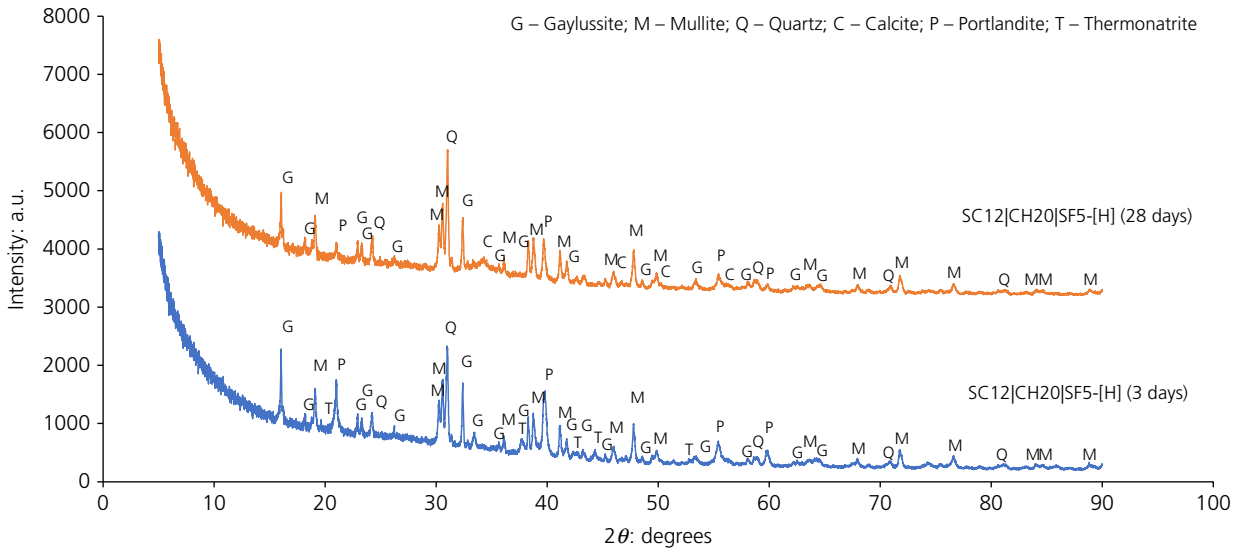


**Figure 5.** XRD patterns of SC12|CH20|SF5-[H] cement paste

Fly ash consists of an amorphous phase and stable but unreactive crystalline phases such as mullite and quartz. During reaction, the amorphous phase undergoes alkali activation, while the unreactive phases act as micro-aggregate in the final matrix (Duxson *et al.*, 2005; Kumar *et al.*, 2017). Therefore, mullite ($Al_{4.75}O_{9.63}Si_{1.25}$, powder diffraction file (PDF) # 98-006-6448) and quartz ($SiO_2$, PDF# 98-006-2405) were detected in all of the cement paste samples (Figures 3–5).

Thermonatrite ($Na_2CO_3H_2O$, PDF# 98-000-6293) was observed in SC12|CH10|SF5-[L] and SC12|CH20|SF5-[H] samples at 3 days (Figures 3 and 5) indicating that sodium carbonate was not fully consumed in reactions at early age due to its high initial concentration – 12% of the fly ash mass – in SC12|CH10|SF5-[L] and SC12|CH20|SF5-[H] cements.

Carbonate salt gaylussite ($Na_2Ca(CO_3)_2(H_2O)_5$, PDF# 98-000-4424) was identified in all samples. Gaylussite is formed due to the cation exchange reaction between calcium hydroxide and sodium carbonate (Equation I). This increases the pH of the system through the release of $OH^-$ ions, facilitating dissolution of the fly ash as discussed in the previous section. At a later stage, gaylussite dissolves as a result of the decreasing concentration of $CO_3^{2-}$ ions in the aqueous phase. The carbonate then re-precipitates as calcite, releasing $Na^+$. This correlates with the XRD patterns. For SC12|CH20|SF5-[H] and SC6|CH20|SF5-[M] samples, a notable decrease in the gaylussite peak intensity and increase in the intensity of calcite ($CaCO_3$, PDF# 98-004-0107) peaks were observed from 3 to 28 days (Figures 4 and 5). Gaylussite is a transient phase that decreases/is consumed as more stable carbonates form at later stages, as shown in Equation II (Bernal *et al.*, 2015; Ke *et al.*, 2016; Yuan *et al.*, 2017). Once the $CO_3^{2-}$ ions have been largely exhausted, the activation reaction proceeds similarly to sodium hydroxide (NaOH)-activated systems (Bernal *et al.*, 2015). Increased pH is one of the reasons for the high compressive strength of SC12|CH20|SF5-[H] and SC6|CH20|SF5-[M] cements. It should be noted that the gaylussite peak intensity increased from 3 to 28 days for SC12|CH10|SF5-[L] (Figure 3), and the formation of calcite was very limited. This indicates that the pH of the system would be lower compared to SC12|CH20|SF5-[H] and SC6|CH20|SF5-[M], which correlates with the low compressive strength gained by SC12|CH10|SF5-[L] cement (Figure 1).

$$\text{I.}\quad 5H_2O + 2Na^+ + Ca^{2+} + 2CO_3^{2-} \rightarrow \underset{\text{(gaylussite)}}{Na_2Ca(CO_3)_2{\cdot}5H_2O}$$

$$\text{II.}\quad Na_2Ca(CO_3)_2{\cdot}5H_2O \rightarrow CaCO_3 + 2Na^+ + 2CO_3^{2-} + 5H_2O$$

Progressive consumption of calcium hydroxide ($Ca(OH)_2$, PDF# 98-020-2220) can be observed, especially in samples SC6|CH20|SF5-[M] and SC12|CH20|SF5-[H], with a decrease in peak intensity of portlandite over time (Figures 3–5). This can be attributed to the cation exchange reaction forming gaylussite and calcite, as well as lime-consuming C–S–H formation (Jeon *et al.*, 2015).

The formation of hydrotalcite ($C_{0.167}H_3Al_{0.333}Mg_{0.667}O_{3.001}$, PDF# 98-008-1963) was only observed in the SC6|CH20|SF5-[M] cement paste.

### SEM analysis

Secondary electron (SE) images of SC12|CH10|SF5-[L], SC6|CH20|SF5-[M] and SC12|CH20|SF5-[H] samples at different

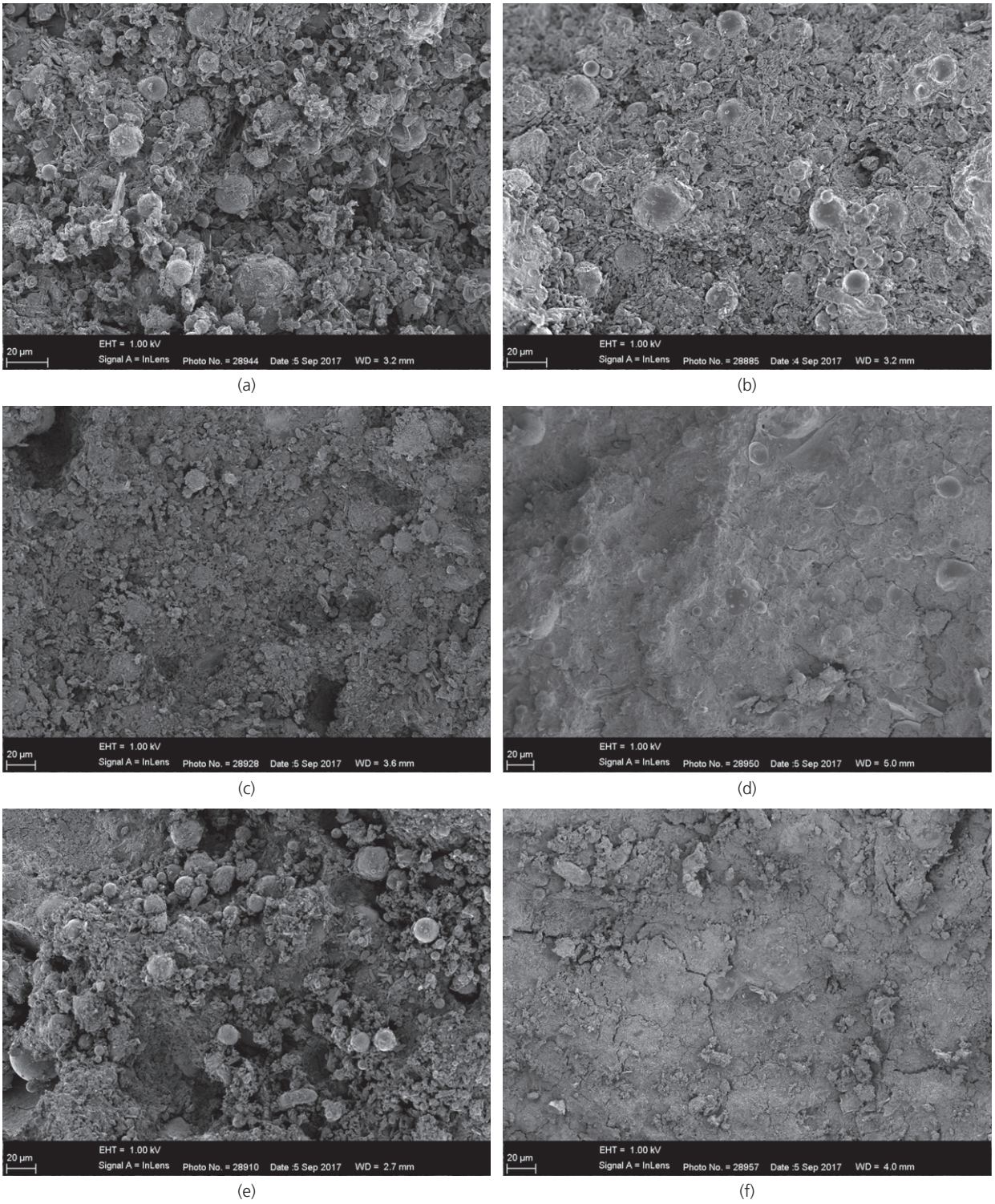


**Figure 6.** SE images at 3 days: (a) SC12|CH10|SF5-[L]; (c) SC6|CH20|SF5-[M]; (e) SC12|CH20|SF5-[H] and at 28 days: (b) SC12|CH10|SF5-[L]; (d) SC6|CH20|SF5-[M]; (f) SC12|CH20|SF5-[H]

curing ages are shown in Figure 6. The SC12|CH20|SF5-[H] cement paste had a noticeable amount of unreacted particles at 3 days (Figure 6(e)). The SC12|CH10|SF5-[L] cement paste showed similar characteristics at 3 days, but the amount of unreacted fly ash particles was even more prominent (Figure 6(a)). However, the SC6|CH20|SF5-[M] cement paste had a more developed

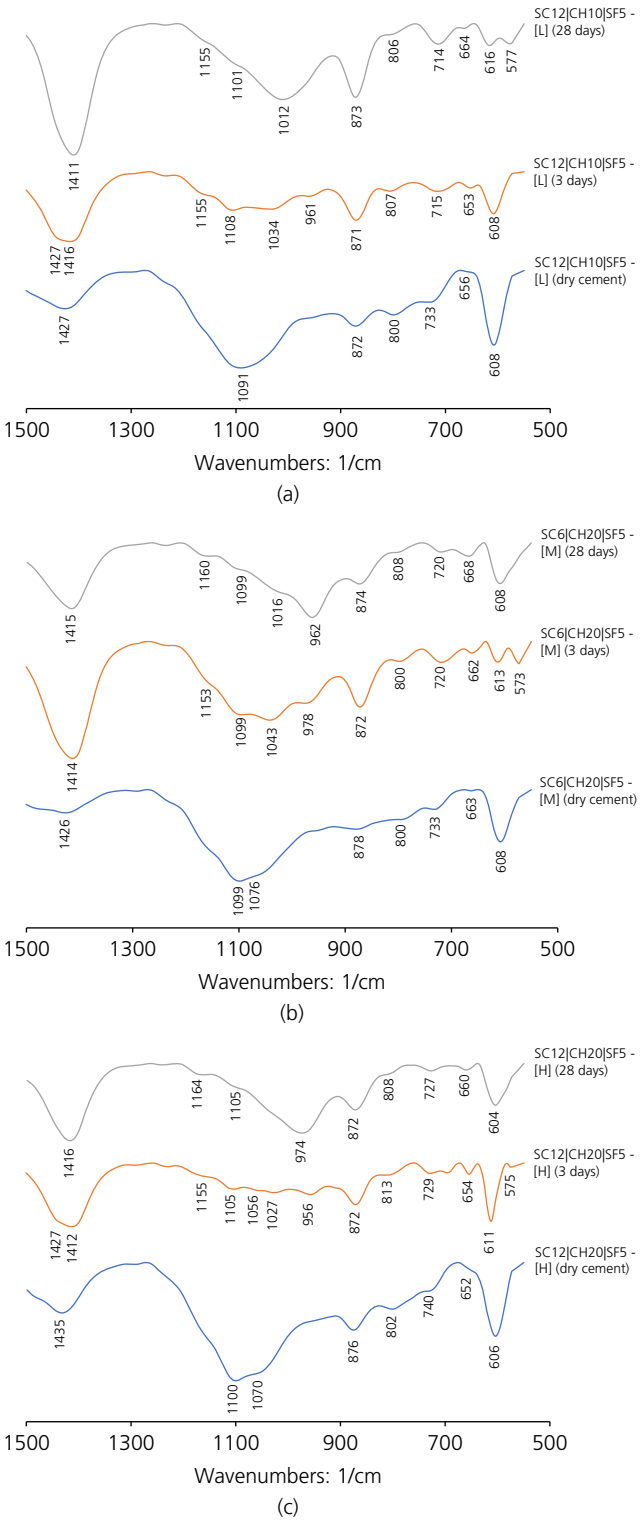


**Figure 7.** FTIR spectra: (a) SC12|CH10|SF5-[L]; (b) SC6|CH20|SF5-[M]; (c) SC12|CH20|SF5-[H]

microstructure at the same age, with a significantly lower amount of unreacted particles (Figure 6(c)), which correlates with the compressive strength results at 3 days (Figure 1).

At 28 days, SC12|CH20|SF5-[H] cement paste went through the most prominent transformation, as most of the unreacted particles observed at 3 days had reacted to form a dense amorphous microstructure (Figure 6(f)). As a result, SC12|CH20|SF5-[H] cement paste showed a significant strength increase, reaching 44.2 MPa at 28 days (Figure 1). In contrast, the microstructure of SC12|CH10|SF5-[L] cement paste did not develop substantially between 3 and 28 days (Figure 6(b)). There were still copious amounts of unreacted fly ash particles, indicating a low dissolution rate, and hence significantly lower strength (Figure 1). SC6|CH20|SF5-[M] cement paste developed similarly to SC12|CH20|SF5-[H], but still contained some unreacted particles (Figure 6(d)). This shows that it did not undergo a large dissolution phase, unlike sample SC12|CH20|SF5-[H], which resulted in lower compressive strength at 28 days in comparison to SC12|CH20|SF5-[H] cement paste (Figure 1).

## FTIR analysis

Figure 7 represents the FTIR spectra from wavenumber section 1500 to 500 $cm^{-1}$ of SC12|CH10|SF5-[L], SC6|CH20|SF5-[M] and SC12|CH20|SF5-[H] cements and cement pastes at different ages. Besides some minor broad humps noticed in the region from 3600 to 3500 $cm^{-1}$, which can be attributed to the strength vibration of –OH (Jang and Lee, 2016), there were no noticeable changes from 4000 to 1500 $cm^{-1}$ and thus this is not included.

There are significant peaks occurring in the region 1435 to 1411 $cm^{-1}$ in all samples, as well as a smaller peak around the 878–871 $cm^{-1}$ region. Those peaks can be associated with stretching vibrations of C = O in $CO_3^{2-}$ anions, which confirms the presence of carbonate species (Abdel-Gawwad and Abo-El-Enein, 2016; Kumar *et al.*, 2017; Lee *et al.*, 2017; Peyne *et al.*, 2017; Shekhovtsova, 2015). At 3 days, a broad peak in the main wavenumbers for carbonate groups (1435–1411 $cm^{-1}$) in SC12|CH10|SF5-[L] and SC12|CH20|SF5-[H] cement pastes indicates the presence of carbonates with different structures, which agrees with the XRD results (Król *et al.*, 2018). Gaylussite and thermonatrite were identified in SC12|CH10|SF5-[L] and SC12|CH20|SF5-[H] cement pastes at 3 days (Figures 3 and 5).

For all cement paste samples, the FTIR spectra have either bands or shoulders at 1164–1153 and 1108–1099 $cm^{-1}$ regions and a double band, which would be visible only at a very high magnification, at the 813–800 $cm^{-1}$ region. These are assigned to quartz in fly ash (Król *et al.*, 2018). The bands and shoulders at 1164–1153 and 1108–1099 $cm^{-1}$ regions would also overlap with bands associated with mullite in the fly ash (Beran *et al.*, 2001).

Spectral bands at 740–714, 668–652, 616–608 and 577–573 $cm^{-1}$ regions occur in all samples and were assigned

to the mullite present in the fly ash (Beran *et al.*, 2001; Schroeder and Lyons, 1966).

The FTIR spectra of all dry cements have an absorbance band around 1100 $cm^{-1}$ wavenumber, with a shoulder at around 1070 $cm^{-1}$. This is attributed to the asymmetric stretching vibration mode of Si–O–T (T = tetrahedral Si or Al) indicating the presence of silica fume and fly ash in the cement compositions. For all investigated samples, this main band shifted to a lower wavenumber after alkaline activation. This is known to be a common occurrence in fly ash alkali-activated materials as it represents the extent of the reaction (De Vargas *et al.*, 2014; Jang and Lee, 2016; Siyal *et al.*, 2016).

For SC12|CH20|SF5-[H], the main band in the cement appears at 1070–1100 $cm^{-1}$ and shifted to 1056 (shoulder), 1027 and 956 $cm^{-1}$ at 3 days and then to 974 $cm^{-1}$ at 28 days (Figure 7(c)). The initial shift to the lower frequencies indicates the formation of sodium aluminosilicate hydrate (N–A–S–H) (1027 $cm^{-1}$) and calcium silicate hydrate (C–A–S–H) (956 $cm^{-1}$) gels (García-Lodeiro *et al.*, 2011; Yu *et al.*, 1999). The shoulder at 1056 $cm^{-1}$ can be assigned to a silica-rich gel (García-Lodeiro *et al.*, 2008). At a later stage, only one strong band at 974 $cm^{-1}$ wavenumber can be observed. The shift from 1056 and 1027 to 974 $cm^{-1}$ indicates consumption of the silica-rich gel and degradation of N–A–S–H gel in favour of formation of C–A–S–H gel (García-Lodeiro *et al.*, 2008, 2011). The shift from 956 to 974 $cm^{-1}$ shows an increase in Si/Al ratio and the degree of polymerisation of the C–A–S–H gel (García-Lodeiro *et al.*, 2008; Yu *et al.*, 1999).

For SC6|CH20|SF5-[M], the main band at 1099 $cm^{-1}$ and shoulder at 1076 $cm^{-1}$ moved to 1043 and 978 $cm^{-1}$ at 3 days and then to 1016 and 962 $cm^{-1}$ at 28 days (Figure 7(b)). The bands at 1043 and 1016 $cm^{-1}$ are assigned to formation of N–A–S–H gel (García-Lodeiro *et al.*, 2011), while bands at 978 and 962 $cm^{-1}$ represent C–A–S–H gel (García-Lodeiro *et al.*, 2008, 2011; Yu *et al.*, 1999). Therefore, N–A–S–H and C–A–S–H gels coexist in SC6|CH20|SF5-[M] cement paste. The shift in the C–A–S–H band to a lower number with time indicates that the degree of polymerisation of the C–A–S–H gel decreases, while the calcium uptake in the C–A–S–H gel structure increases (García-Lodeiro *et al.*, 2008; Yu *et al.*, 1999).

For SC12|CH10|SF5-[L], the main band at 1091 $cm^{-1}$ shifted to 1034 and 961 $cm^{-1}$ at 3 days but then moved to 1012 $cm^{-1}$ at 28 days (Figure 7(a)). Therefore, this represents formation of N–A–S–H (1034 $cm^{-1}$) and C–A–S–H (961 $cm^{-1}$) gels at early age and degradation of the C–A–S–H gel in favour of formation of N–A–S–H gel at 28 days (García-Lodeiro *et al.*, 2011). The N–A–S–H bands appear at wavenumbers higher than 1000 $cm^{-1}$, indicating a possible mixture of N–A–S–H gel and a silica-rich gel (García-Lodeiro *et al.*, 2008).

**Table 8.** Greenhouse emissions

| Cement ID | Emissions: kg $CO_2$-e/kg |
|---|---|
| SC12\|CH20\|SF15 | 0.151 |
| SC12\|CH20\|SF5 | 0.160 |
| SC12\|CH10\|SF15 | 0.115 |
| SC12\|CH10\|SF5 | 0.122 |
| SC6\|CH20\|SF15 | 0.132 |
| SC6\|CH20\|SF5 | 0.141 |
| SC6\|CH10\|SF15 | 0.092 |
| SC6\|CH10\|SF5 | 0.098 |
| SC12\|CH15\|SF10 | 0.137 |
| SC6\|CH15\|SF10 | 0.116 |
| SC9\|CH20\|SF10 | 0.146 |
| SC9\|CH10\|SF10 | 0.107 |
| SC9\|CH15\|SF15 | 0.123 |
| SC9\|CH15\|SF5 | 0.131 |
| SC9\|CH15\|SF10 | 0.127 |

The initial shift to a lower wavenumber (956 $cm^{-1}$) at 3 days in SC12|CH20|SF5-[H] cement paste compared to other two cement pastes can be attributed to a higher pH in the system and higher calcium uptake in the C–A–S–H gel structure (García-Lodeiro *et al.*, 2008; Yu *et al.*, 1999). At 28 days, reaction products of SC12|CH20|SF5-[H] cement paste comprise only C–A–S–H gel, whereas N–A–S–H and C–A–S–H gels coexist in SC6|CH20|SF5-[M] cement paste and the main reaction product in SC12|CH10|SF5-[L] cement paste is N–A–S–H gel. This can also be an indication of a higher pH developing in SC12|CH20|SF5-[H] cement paste compared to SC6|CH20|SF5-[M] and SC12|CH10|SF5-[L] cement pastes (García-Lodeiro *et al.*, 2011).

### Greenhouse gas emissions

The greenhouse gas emissions associated with the developed one-part fly ash alkali-activated cements are shown in Table 8. The emission values presented are calculated based on the emissions of the raw materials (Table 2) and do not include emissions associated with production of the cements (transportation, blending, packaging, etc.).

For comparison, one of the most sustainable binders used in the construction industry at the moment, blended Portland cement containing 65% of ground granulated blast furnace slag, has greenhouse gas emissions equal to 0.465 kg $CO_2$-e/kg (greenhouse gas emission factors of 0.187 kg $CO_2$-e/kg for slag and 0.982 kg $CO_2$-e/kg for Portland cement were used (Infrastructure Sustainability Council of Australia, 2021)). The developed novel cements do not need an accelerated curing at elevated temperatures, which is typically required for fly ash alkali-activated cements and would further contribute to the greenhouse gas emissions. Therefore, the global warming potential of the novel one-part fly ash alkali-activated cements is 65–80% lower compared to highly blended Portland cement.

### Study limitations and future research

There are a few limitations in this study. First, the evolution of pH in the novel one-part fly ash alkali-activated cement pastes was not measured and will be investigated in future research to confirm its role in the microstructural development of the cements. Second, a further validation and optimisation of the statistical model would be beneficial for compressive strength development predictions. Third, standard properties of the developed cements – setting times, shrinkage and so on – will be investigated in the future. It is also important to design mortars/concretes utilising the novel cements and study their standard properties, including durability performance. These are critical for conformance to relevant specifications and standards for facilitating acceptance of the novel one-part fly ash alkali-activated cements in the construction industry in the future.

## Conclusions

Under ambient curing conditions, the developed novel one-part fly ash alkali-activated cements gained compressive strength up to 11.0 and 44.2 MPa at 3 and 28 days, respectively. Sodium carbonate and calcium hydroxide were the main factors that positively affected the 28 day mechanical strength of the cements. Silica fume also showed a positive effect on the strength development, although the magnitude of the effect was less significant.

Mineralogical and microstructural investigations revealed that the cation exchange reaction between calcium hydroxide and sodium carbonate was the key element in the microstructural development of the cements. Gaylussite and subsequently calcite were formed during the reaction, releasing hydroxide ions, which would increase the pH of the system, facilitating activation. Further experimental investigation is required to confirm the pH increase and actual pH values in the novel one-part fly ash alkali-activated cement pastes depending on the cement composition.

The developed novel one-part fly ash alkali-activated cements use low-impact activators that are cheaper, easier to handle and have less environmental impact than the commonly used activators, sodium hydroxide and sodium silicate. The activators used in this study are not hygroscopic in nature, allowing for intermixing and storage in bags just like ordinary Portland cement. With further investigation and proper standards set up, this type of binding system could prove to be a low-carbon alternative to blended Portland cements and drive its acceptance within the construction industry.

## Acknowledgements

The authors would like to thank Wiebke Grote and Jeanette Dykstra for their assistance in performing the XRD and XRF analysis was used to determine chemical composition of raw materials. The assistance with the SEM studies provided by André Botha and Alan Hall is gratefully acknowledged.

### REFERENCES

Abdalqader AF, Jin F and Al-Tabbaa A (2016) Development of greener alkali-activated cement: utilisation of sodium carbonate for activating slag and fly ash mixtures. *Journal of Cleaner Production* **113**: 66–75, https://doi.org/10.1016/j.jclepro.2015.12.010.

Abdel-Gawwad HA and Abo-El-Enein SA (2016) A novel method to produce dry geopolymer cement powder. *HBRC Journal* **12(1)**: 13–24, https://doi.org/10.1016/j.hbrcj.2014.06.008.

Assi LN, Deaver E, El Batanouny MK and Ziehl P (2016) Investigation of early compressive strength of fly ash-based geopolymer concrete. *Construction and Building Materials* **112**: 807–815, https://doi.org/10.1016/j.conbuildmat.2016.03.008.

Beran A, Voll D and Schneider H (2001) Dehydration and structural development of mullite precursors: an FTIR spectroscopic study. *Journal of the European Ceramic Society* **21(14)**: 2479–2485, https://doi.org/10.1016/S0955-2219(01)00265-5.

Bernal SA, Provis JL, Myers RJ, San Nicolas R and van Deventer JSJ (2015) Role of carbonates in the chemical evolution of sodium carbonate-activated slag binders. *Materials and Structures* **48**: 517–529, https://doi.org/10.1617/s11527-014-0412-6.

Department of Industry, Science, Energy and Resources (2021) *National Greenhouse Accounts Factors*. Australian National Greenhouse Accounts. See https://www.industry.gov.au/sites/default/files/August%202021/document/national-greenhouse-accounts-factors-2021.pdf (accessed 01/11/2021).

De Vargas SA, Dal Molin DCC, Masuero ÂB *et al.* (2014) Strength development of alkali-activated fly ash produced with combined NaOH and $Ca(OH)_2$ activators. *Cement and Concrete Composites* **53**: 341–349, https://doi.org/10.1016/j.cemconcomp.2014.06.012.

Dutta D, Thokchom S, Ghosh P and Ghosh S (2010) Effect of silica fume additions on porosity of fly ash geopolymers. *Journal of Engineering and Applied Science* **5(10)**: 74–79.

Duxson P, Provis JL, Lukey GC *et al.* (2005) Understanding the relationship between geopolymer composition, microstructure and mechanical properties. *Colloids and Surfaces A: Physicochemical and Engineering Aspects* **269(1–3)**: 47–58, https://doi.org/10.1016/j.colsurfa.2005.06.060.

Duxson P, Fernández-Jiménez A, Provis JL *et al.* (2007) Geopolymer technology: the current state of the art. *Journal of Materials Science* **42**: 2917–2933, https://doi.org/10.1007/s10853-006-0637-z.

Eskom (2021) *Ash Management in Eskom*. See https://www.eskom.co.za/AboutElectricity/FactsFigures/CO%20%20Coal/CO%200004%20%20Ash%20Management%20Rev%2015.pdf (accessed 28/10/2021).

Fernández-Jiménez A and Puertas F (2003) Effect of activator mix on the hydration and strength behaviour of alkali-activated slag cements. *Advances in Cement Research* **15(3)**: 129–136, https://doi.org/10.1680/adcr.2003.15.3.129.

Fraay ALA, Bijen JM and de Haan YM (1989) The reaction of fly ash in concrete a critical examination. *Cement and Concrete Research* **19(2)**: 235–246, https://doi.org/10.1016/0008-8846(89)90088-4.

García-Lodeiro I, Fernández-Jiménez A, Blanco MT and Palomo A (2008) FTIR Study of the sol–gel synthesis of cementitious gels: C–S–H and N–A–S–H. *Journal of Sol-Gel Science and Technology* **45**: 63–72, https://doi.org/10.1007/s10971-007-1643-6.

García-Lodeiro I, Palomo A, Fernández-Jiménez A and MacPhee DE (2011) Compatibility studies between N-A-S-H and C-A-S-H gels. Study in the ternary diagram $Na_2O$–CaO-$Al_2O_3$-$SiO_2$-$H_2O$. *Cement and Concrete Research* **41(9)**: 923–931, https://doi.org/10.1016/j.cemconres.2011.05.006.

Habert G, D'Espinose De Lacaillerie JB and Roussel N (2011) An environmental evaluation of geopolymer based concrete production: reviewing current research trends. *Journal of Cleaner Production* **19(11)**: 1229–1238, https://doi.org/10.1016/j.jclepro.2011.03.012.

Huang S and Cheng J (1986) Kinetic of reaction in the system fly ash-$Ca(OH)_2$-$H_2O$. *Journal of the Chinese Ceramic Society* **14**: 191–197.

Infrastructure Sustainability Council of Australia (2021) See https://www.iscouncil.org/ (accessed 21/11/2021).

Ismail I, Bernal SA, Provis JL, Hamda S and van Deventer JSJ (2013a) Drying-induced changes in the structure of alkali-activated pastes. *Journal of Materials Science* **48**: 3566–3577, https://doi.org/10.1007/s10853-013-7152-9.

Ismail I, Bernal SA, Provis JL *et al.* (2013b) Influence of fly ash on the water and chloride permeability of alkali-activated slag mortars and concretes. *Construction and Building Materials* **48**: 1187–1201, https://doi.org/10.1016/j.conbuildmat.2013.07.106.

Jambhulkar HP, Shaikh SMS and Kumar MS (2018) Fly ash toxicity, emerging issues and possible implications for its exploitation in agriculture; Indian scenario: a review. *Chemosphere* **213**: 333–334, https://doi.org/10.1016/j.chemosphere.2018.09.045.

Jang JG and Lee HK (2016) Effect of fly ash characteristics on delayed high-strength development of geopolymers. *Construction and Building Materials* **102(1)**: 260–269, https://doi.org/10.1016/j.conbuildmat.2015.10.172.

Jeon D, Jun Y, Jeong Y and Oh JE (2015) Microstructural and strength improvements through the use of $Na_2CO_3$ in a cementless $Ca(OH)_2$-activated Class F fly ash system. *Cement and Concrete Research* **67**: 215–225, https://doi.org/10.1016/j.cemconres.2014.10.001.

Jin F and Al-Tabbaa A (2015) Strength and drying shrinkage of slag paste activated by sodium carbonate and reactive MgO. *Construction and Building Materials* **81**: 58–65, https://doi.org/10.1016/j.conbuildmat.2015.01.082.

Ke X, Bernal SA and Provis JL (2016) Controlling the reaction kinetics of sodium carbonate-activated slag cements using calcined layered double hydroxides. *Cement and Concrete Research* **81**: 24–37, https://doi.org/10.1016/j.cemconres.2015.11.012.

Khale D and Chaudhary R (2007) Mechanism of geopolymerization and factors influencing its development: a review. *Journal of Materials Science* **42**: 729–746, https://doi.org/10.1007/s10853-006-0401-4.

Król M, Rożek P, Chlebda D and Mozgawa W (2018) Influence of alkali metal cations/type of activator on the structure of alkali-activated fly ash – ATR-FTIR studies. *Spectrochimica Acta Part A: Molecular and Biomolecular Spectroscopy* **198**: 33–37, https://doi.org/10.1016/j.saa.2018.02.067.

Kumar S, Mucsi G, Kristály F and Pekker P (2017) Mechanical activation of fly ash and its influence on micro and nano-structural behaviour of resulting geopolymers. *Advanced Powder Technology* **28(3)**: 805–813, https://doi.org/10.1016/j.apt.2016.11.027.

Lee NK, Koh KT, Kim MO, An GH and Ryu GS (2017) Physicochemical changes caused by reactive MgO in alkali-activated fly ash/slag blends under accelerated carbonation. *Ceramics International* **43(15)**: 12490–12496, https://doi.org/10.1016/j.ceramint.2017.06.119.

Li D, Chen Y, Shen J, Su J and Wu X (2000) The influence of alkalinity on activation and microstructure of fly ash. *Cement and Concrete Research* **30(6)**: 881–886, https://doi.org/10.1016/S0008-8846(00)00252-0.

Li C, Sun H and Li L (2010) A review: the comparison between alkali-activated slag (Si + Ca) and metakaolin (Si + Al) cements. *Cement and Concrete Research* **40(9)**: 1341–1349, https://doi.org/10.1016/j.cemconres.2010.03.020.

McLellan BC, Williams RP, Lay J, van Riessen A and Corder GD (2011) Costs and carbon emissions for geopolymer pastes in comparison to ordinary Portland cement. *Journal of Cleaner Production* **19 (9–10)**: 1080–1090, https://doi.org/10.1016/j.jclepro.2011.02.010.

Montgomery DC and Runger GC (2011) *Applied Statistics and Probability for Engineers*, 5th edn. John Wiley & Sons, Hoboken, NJ, USA.

Mustafa Al Bakria AM, Kamarudin H, Bin Hussain M *et al.* (2011) The effect of curing temperature on physical and chemical properties of geopolymers. *Physics Procedia* **22**: 286–291, https://doi.org/10.1016/j.phpro.2011.11.045.

National Planning Commission (2017) *Our Future - Make It Work, National Development Plan 2030, Executive Summary*. See https://www.gov.za/sites/default/files/ExecutiveSummary-NDP2030-Ourfuture-makeitwork.pdf (accessed 12/12/2019).

Olivia M and Nikraz H (2012) Properties of fly ash geopolymer concrete designed by Taguchi method. *Materials & Design* **26**: 191–198, https://doi.org/10.1016/j.matdes.2011.10.036.

Part WK, Ramli M and Cheah CB (2015) An overview on the influence of various factors on the properties of geopolymer concrete derived from industrial by-products. *Construction and Building Materials* **77**: 370–395, https://doi.org/10.1016/j.conbuildmat.2014.12.065.

Peyne J, Gautron J, Doudeau J, Joussein E and Rossignol S (2017) Influence of calcium addition on calcined brick clay based geopolymers: a thermal and FTIR spectroscopy study. *Construction and Building Materials* **152**: 794–803, https://doi.org/10.1016/j.conbuildmat.2017.07.047.

Rangan V (2010) Fly ash-based geopolymer concrete. In *Proceedings of International Workshop on Geopolymer Cement and Concrete* (Jeyasehar CA and Thirugnanasambandam S (eds)). Allied Publishers Pvt Ltd., Annamalainagar, India, pp. 68–106.

Rashad AM (2013) A comprehensive overview about the influence of different additives on the properties of alkali-activated slag – a guide for civil engineer. *Construction and Building Materials* **47**: 29–55, https://doi.org/10.1016/j.conbuildmat.2013.04.011.

Rashad AM and Khalil MH (2013) A preliminary study of alkali-activated slag blended with silica fume under the effect of thermal loads and thermal shock cycles. *Construction and Building Materials* **40**: 522–532, https://doi.org/10.1016/j.conbuildmat.2012.10.014.

Ryu GS, Lee YB, Koh KT and Chung YS (2013) The mechanical properties of fly ash-based geopolymer concrete with alkaline activators. *Construction and Building Materials* **47**: 409–418, https://doi.org/10.1016/j.conbuildmat.2013.05.069.

SABS (South African Bureau of Standards) (2006) *SANS 50196-1: Methods of testing cement Part 1: Determination of strength*. South African National Standards, Pretoria, South Africa.

Sato T and Beaudoin JJ (2011) Effect of nano-$CaCO_3$ on hydration of cement containing supplementary cementitious materials. *Advances in Cement Research* **23(1)**: 33–43, https://doi.org/10.1680/adcr.9.00016.

Sayed M and Zeedan SR (2012) Green binding material using alkali activated blast furnace slag with silica fume. *HBRC Journal* **8(3)**: 177–184, https://doi.org/10.1016/j.hbrcj.2012.10.003.

Schroeder RA and Lyons LL (1966) Infra-red spectra of the crystalline inorganic aluminates. *Journal of Inorganic and Nuclear Chemistry* **28(5)**: 1155–1163, https://doi.org/10.1016/0022-1902(66)80441-4.

Shekhovtsova J (2015) *Using South Africa Fly Ash as A Component of Alkali-Activated Binder*. PhD thesis, University of Pretoria, Pretoria, South Africa.

Shekhovtsova J, Kearsley EP and Kovtun M (2014) Effect of activator dosage, water-to-binder-solids ratio, temperature and duration of elevated temperature curing on the compressive strength of alkali-activated fly ash cement pastes. *Journal of the South African Institution of Civil Engineers* **56(3)**: 44–52.

Shi C and Day RL (2000) Pozzolanic reaction in the presence of chemical activators: part I. Reaction kinetics. *Cement and Concrete Research* **30(1)**: 51–58, https://doi.org/10.1016/S0008-8846(99)00205-7.

Silva SVA, Arachchi JNJK, Wijewardena CL and Nanayakkara SM (2013) Development of fly ash based geopolymer concrete. *17th Annual*

*Research Symposium on Excellence in Research, Excelling A Nation*. University of Moratuwa, Moratuwa, Sri Lanka, pp. 75–77.

Siyal AA, Azizli KA, Man Z, Ismail L and Khan MI (2016) Geopolymerization kinetics of fly ash based geopolymers using JMAK model. *Ceramics International* **42(14)**: 15575–15584, https://doi.org/10.1016/j.ceramint.2016.07.006.

Songpiriyakij S, Pulngern T, Pungpremtrakul P and Jutarapitakkul C (2011) Anchorage of steel bars in concrete by geopolymer paste. *Materials & Design* **32(5)**: 3021–3028, https://doi.org/10.1016/j.matdes.2011.01.048.

StatEase Inc. (2021) Design-Expert Software V11, Minneapolis, MN. See https://www.statease.com/docs/v11/contents/analysis/interpretation-of-r-squared/ (accessed 16/11/2021).

Turner LK and Collins FG (2013) Carbon dioxide equivalent ($CO_2$-e) emissions: a comparison between geopolymer and OPC cement concrete. *Construction and Building Materials* **43**: 125–130, https://doi.org/10.1016/j.conbuildmat.2013.01.023.

U.S. Geological Survey (2017) Mineral Commodity Summaries 2017, see https://doi.org/10.3133/70180197 (accessed 22/02/2020).

Yu P, Kirkpatrick RJ, Poe B, McMillan PF and Cong X (1999) Structure of calcium silicate hydrate (C–S–H): near-, mid-, and far-infrared spectroscopy. *Journal of the American Ceramic Society* **82(3)**: 742–748.

Yuan B, Yu QL and Brouwers HJH (2017) Assessing the chemical involvement of limestone powder in sodium carbonate activated slag. *Materials and Structures* **50**: 136, https://doi.org/10.1617/s11527-017-1003-0.

## How can you contribute?

To discuss this paper, please submit up to 500 words to the editor at journals@ice.org.uk. Your contribution will be forwarded to the author(s) for a reply and, if considered appropriate by the editorial board, it will be published as a discussion in a future issue of the journal.